

Atomic origin of minor alloying element effect on glass forming ability of metallic glass

Shan Zhang(张珊), Qingan Li(李庆安), Yong Yang(杨勇), and Pengfei Guan(管鹏飞)

Citation: Chin. Phys. B, 2025, 34 (**3**): 036105. DOI: 10.1088/1674-1056/ada756
Journal homepage: http://cpb.iphy.ac.cn; http://iopscience.iop.org/cpb

What follows is a list of articles you may be interested in

Effect of Y element on atomic structure, glass forming ability, and magnetic properties of FeBC alloy

Jin-Hua Xiao(肖晋桦), Da-Wei Ding(丁大伟), Lin Li(李琳), Yi-Tao Sun(孙奕韬), Mao-Zhi Li(李茂枝), and Wei-Hua Wang(汪卫华)
Chin. Phys. B, 2024, 33 (**7**): 076101. DOI: 10.1088/1674-1056/ad3dd4

Universal basis underlying temperature, pressure and size induced dynamical evolution in metallic glass-forming liquids

H P Zhang(张华平), B B Fan(范蓓蓓), J Q Wu(吴佳琦), and M Z Li(李茂枝)
Chin. Phys. B, 2024, 33 (**1**): 016101. DOI: 10.1088/1674-1056/acf994

Structural origin for composition-dependent nearest atomic distance in Cu-Zr metallic glass

Chi Zhang(张驰), Hua-Shan Liu(刘华山), and Hai-Long Peng(彭海龙)
Chin. Phys. B, 2023, 32 (**11**): 116101. DOI: 10.1088/1674-1056/acce99

Non-monotonic temperature evolution of nonlocal structure-dynamics correlation in CuZr glass-forming liquids

W J Jiang(江文杰) and M Z Li(李茂枝)
Chin. Phys. B, 2021, 30 (**7**): 076102. DOI: 10.1088/1674-1056/abf113

Heredity of clusters in the rapidly cooling processes of Al-doped $Zr_{50}Cu_{50}$ melts and its correlation with the glass-forming ability

Dadong Wen(文大东), Yonghe Deng(邓永和), Ming Gao(高明), and Zean Tian(田泽安)
Chin. Phys. B, 2021, 30 (**7**): 076101. DOI: 10.1088/1674-1056/abea93

Atomic origin of minor alloying element effect on glass forming ability of metallic glass

Shan Zhang(张珊)[1,2], Qingan Li(李庆安)[1], Yong Yang(杨勇)[2,†], and Pengfei Guan(管鹏飞)[1,3,‡]

[1] *Beijing Computational Science Research Center, Beijing* 100193, *China*
[2] *Department of Mechanical Engineering, College of Engineering, City University of Hong Kong, Tat Chee Avenue, Kowloon Tong, Kowloon, Hong Kong, China*
[3] *Advanced Interdisciplinary Sciences Research (AiR) Center, Ningbo Institute of Materials Technology and Engineering, Chinese Academy of Sciences, Ningbo* 315201, *China*

(Received 17 October 2024; revised manuscript received 25 December 2024; accepted manuscript online 8 January 2025)

The glass-forming ability (GFA) of metallic glasses is a key scientific challenge in their development and application, with compositional dependence playing a crucial role. Experimental studies have demonstrated that the addition of specific minor elements can greatly enhance the GFA of parent alloys, yet the underlying mechanism remains unclear. In this study, we use the ZrCuAl system as a model to explore how the addition of minor Al influences the crystallization rate by modulating the properties of the crystal–liquid interface, thereby affecting the GFA. The results reveal that the minor addition of Al significantly reduces the crystal growth rate, a phenomenon not governed by particle density fluctuations at the interface. The impact of minor element additions extends beyond a modest increase in crystal-unfavorable motifs in the bulk supercooled liquid. More importantly, it leads to a significant enrichment of these motifs at the crystal-supercooled liquid interface, forming a dense topological network of crystal-unfavorable structures that effectively prevent the growth of the crystalline interface and enhance GFA. Our results provide valuable insights for the design and development of high-performance metallic glasses.

Keywords: metallic glass, glass forming ability, interface structure, molecular dynamics (MD)

PACS: 61.43.Fs, 68.35.Ct, 81.05.Kf

DOI: 10.1088/1674-1056/ada756 **CSTR:** 32038.14.CPB.ada756

1. Introduction

Metallic glasses (MGs) are non-equilibrium metastable systems that have found significant industrial applications due to their excellent strength and high hardness.[1–4] They also exhibit excellent resistance against wear and corrosion,[5,6] remarkable irradiation resistance,[7] and demonstrate superior performance in catalysis, magnetism, and electronics.[8–10] In the field of materials science, understanding the glass forming ability (GFA) of materials holds great importance and has consistently been a focal point of research interest, driven by its significance. The GFA of a material is primarily influenced by its chemical composition, and theoretical models have been developed to predict and explain GFA,[11–15] providing a fundamental understanding of the underlying mechanisms.[16–18]

However, despite notable advancements, accurately explaining the GFA of materials continues to be a challenging task due to the complex nature of glass transition. Recent studies have highlighted the significant influence of minor alloying elements on GFA.[19] Experimental investigations have demonstrated that the addition of a small percentage of minor elements to various MGs often leads to substantial improvements in both their GFA and properties.[20–22] For example, the GFA of the CuZr-based bulk metallic glasses (BMGs) can be dramatically enhanced by incorporating minor element additions, resulting in large diameters of up to 15 mm.[23,24] Similarly, the critical diameter of Ce–Al–Cu glassy rods can be significantly increased from 2 mm to at least 3 mm–10 mm by introducing minor amounts of elements, such as Fe, Co, Ni, Nb, Zn, and Si.[25] In the case of $Gd_{55}Co_{20}Al_{25}$ MG, the critical diameter increased from 2 mm to 7 mm through the addition of 0.5-at.% Si, while maintaining the magnetocaloric effect.[26] Furthermore, the inclusion of minor elements in MGs has been found to enhance plasticity[27] and saturation magnetization.[28] Despite the progress made in understanding the impact of minor elements on GFA,[26,29–31] the atomic origin of the effect of minor alloying element remains elusive.

In this work, we employed molecular dynamics (MD) simulations to elucidate the atomic-scale mechanisms behind the enhancement of GFA through the addition of minor Al elements in CuZr-based MGs. As the Al content increases from 0 to 8%, the crystallization rate declines rapidly from 0.2 m/s to 0.02 m/s. Through the analysis of the atomic structure at the liquid–crystal interface during crystallization, we discovered that the addition of minor Al to CuZr-based MGs alters the local topological structure order while almost not affecting the

†Corresponding author. E-mail: yongyang@cityu.edu.hk
‡Corresponding author. E-mail: pguan@nimte.ac.cn

© 2025 Chinese Physical Society and IOP Publishing Ltd. All rights, including for text and data mining, AI training, and similar technologies, are reserved.

overall atomic density distribution. This alteration leads to the swift disappearance of the crystal-like structure and the emergence of the local atomic clusters of high fivefold symmetry, resulting in a network of such atomic clusters at the solid–liquid interface that disrupts the continuous pathways necessary for crystal structure formation.

2. Computational details

In our MD simulations, we focused on the (100) and (110) faces of $(ZrCu)_{100-x}Al_x$ alloys with varying Al content ($x = 0$, 2, and 8) to investigate the influence of minor element on crystal growth rate. To carry out these simulations, we utilized the widely used package of Large-scale Atomic/Molecular Massively Parallel Simulator (LAMMPS),[32] employing the embedded atom method potentials,[33] specifically designed for the Cu–Zr–Al alloy system. Our simulation cells had 11520 atoms and the dimensions of approximately 4 nm×4 nm×24 nm, and periodic boundary conditions were applied in all three directions. As depicted in Fig. 1(a), the substrate consisted of a $Zr_{50}Cu_{50}$ ($x = 0$) crystalline solid layer with a thickness of about 4 nm, while the growth layer comprised a supercooled liquid layer of $(ZrCu)_{100-x}Al_x$ ($x = 0$, 2, and 8) with a thickness of 10 nm. To isolate the impact of the crystal/liquid interface on the crystal growth rate, we introduced a vacuum layer of 10-nm along the long axis of the cell. The simulations proceeded as follows: (i) The samples were heated from 900 K to 1200 K using the constant number, pressure, and temperature (NPT) ensemble. (ii) A vacuum layer of 10 nm was established along the z-axis, and the supercooled liquid region ($z = 4$ nm–14 nm) was melted. The entire simulation cell was then under the constant number, volume, and temperature (NVT) condition. At each temperature, the atoms in the bottom 2 nm of the crystalline layer were kept fixed, while the remaining 2 nm served as a buffer-layer. The amorphous layer beyond the 4-nm region was allowed to relax at various temperatures under NVT conditions. After this relaxation, the 2-nm buffer-layer and the amorphous layer relaxed under NVT conditions at the target temperature point. (iii) The samples were relaxed at the melting temperatures to achieve a well-equilibrated crystal/liquid system. (iv) Finally, the crystal growth rates were measured at various temperatures.

3. Results and discussion

3.1. The addition of minor Al elements

According to Ref. [34], the crystal growth rate can be calculated using the equation $v = \dot{V} d_{\mathrm{l}}/N_{\mathrm{l}}(V_{\mathrm{c}} - V_{\mathrm{l}})$, where $\dot{V}$ represents the rate of change in the volume of the simulation cell, d_{l} is the distance of the liquid layer to crystal layer along with the interface normal, N_{l} is the average number of atoms from the liquid to crystal phase, and V_{c} and V_{l} denote the volumes of the crystal and liquid layer, respectively. Figure 1(b) illustrates the crystal growth rates as a function of temperature for different compositions of $(ZrCu)_{100-x}Al_x$ ($x = 0$, 2, and 8) with (110) and (100) surfaces. Notably, the growth rates of two surfaces with the same composition were almost identical. Moreover, the temperature at which the maximum crystal growth rate occurs remains consistent regardless of changes in chemical composition. The addition of Al to the $(ZrCu)_{100-x}Al_x$ alloy significantly reduces the crystal growth rate. Specifically, when the Al content reaches 8%, the crystal growth rate decreases from 0.2 m/s to 0.02 m/s. Additionally, the temperature range for crystallization ($v(T) > 0$) narrows, indicating that $(ZrCu)_{92}Al_8$ exhibits enhanced GFA. In theory,[34] the crystal growth rate can be further described by the following equation:

$$v(T) = k(T)\left[1 - \exp\left(\frac{-\Delta\mu(T)}{k_{\mathrm{B}}T}\right)\right], \tag{1}$$

where $\Delta\mu(T)$ represents the difference in chemical potential between the liquid and crystal phases; k_{B} is the Boltzmann constant; and $k(T)$ is a prefactor that can be determined using the Wilson–Frenkel theory.[35,36] Finally, the crystal growth rate can be formulated as

$$\frac{v(T)\,\sigma^2}{DL} = C\left[1 - \exp\left(\frac{-\Delta\mu(T)}{k_{\mathrm{B}}T}\right)\right]. \tag{2}$$

In this formulation, D represents the diffusion constant, σ is obtained from the position of the first peak in the radial distribution function, and L is the lattice spacing normal to the surface. The term $v(T)\,\sigma^2/(DL)$ signifies the overall number of crystal layers deposited per diffusion time. As shown in Fig. 1(b), the crystallization growth rates of different crystal planes were roughly the same, with similar overall trends. However, as shown in Fig. 1(c), the intrinsic growth rates of the {100} and {110} planes are different. According to Eq. (2), the different intrinsic growth rate of each plane is mainly due to the change in different lattice spacing, related to L. The constant C, which can be extracted from the slope of the fitting lines in Fig. 1(c) with its value depicted in Fig. 2(b), represents the rate of liquid layer addition per diffusion time. Notably, as the Al content increases to 8%, C approaches zero at deeply supercooled temperatures.

Figure 2(a) demonstrates that the addition of Al has minimal impact on the diffusion constant D values for Cu and Zr atoms, except for slight variations at extremely high temperatures. Moreover, the introduction of minor elements has negligible effects on the values of σ and L on both the (110) and (100) surfaces. However, the crucial factor, C, plays a significant role in distinguishing the crystal growth rates. As depicted in Fig. 1(c), the ZrCu alloys reveal a temperature-independent nature of C, which aligns with previous research.[34] In contrast, when Al is added, C exhibits a decrease at lower temperatures on the same surface. Particularly,

when Al comprises 8% of the composition, a notable reduction in the C parameter is observed on the (110) surface at lower temperatures. This substantial deviation in C for $(ZrCu)_{92}Al_8$ suggests unusually sluggish dynamics at lower temperatures.

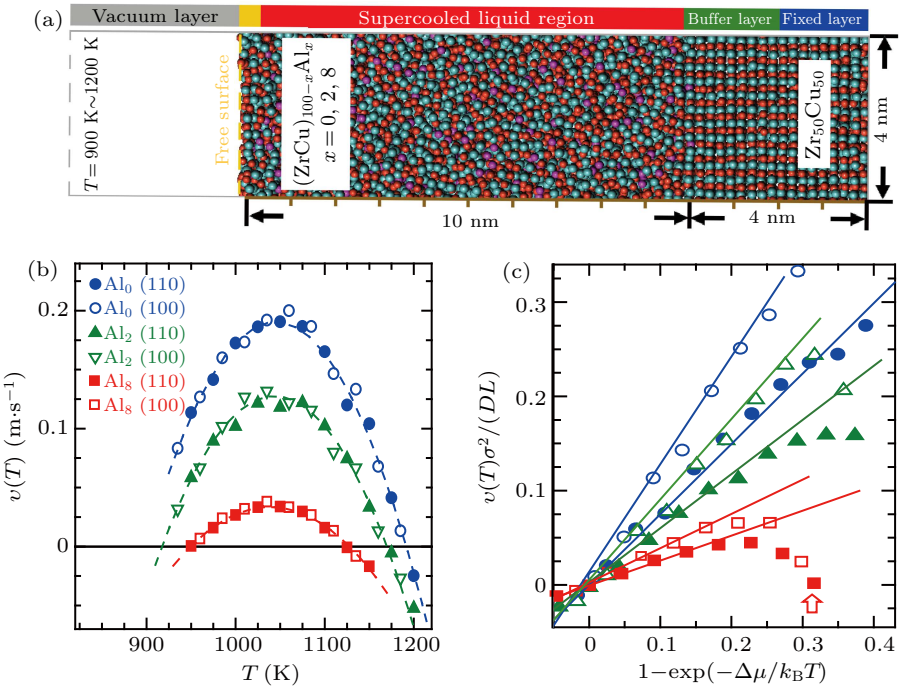


Fig. 1. Panel (a) shows the snapshot of the crystal/liquid interface system. (b) Crystal growth rates for $(ZrCu)_{100-x}Al_x$ ($x = 0$, 2, and 8) with (110) and (100) surface. Panel (c) shows $v(T)\sigma^2/(DL)$ against the $1-\exp(-\Delta\mu(T)/(k_BT))$ for the samples. Solid lines correspond to linear fits. The red arrow signifies the rapid drop of value C (obtained from the slopes) in $(ZrCu)_{92}Al_8$'s (110) surface at the deep supercooled temperature.

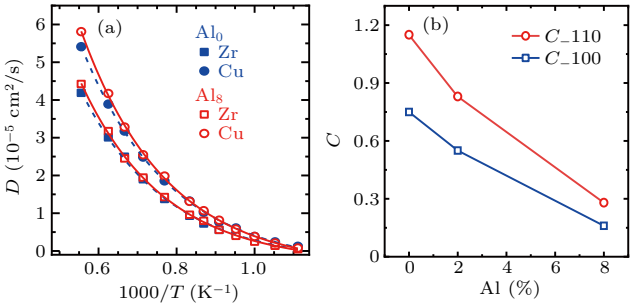


Fig. 2. (a) Diffusion constants of Zr and Cu in $(ZrCu)_{100-x}Al_x$ ($x = 0$, and 8) as a function of temperature. (b) C of the $(ZrCu)_{100-x}Al_x$ ($x = 0$, 2, and 8) for the (110) and (100) surfaces.

3.2. Interface structure analysis

Based on previous studies,[34,37,38] it is clear that the crystal growth rate is influenced by the structure and chemical composition of the crystal/liquid interface. Figures 3(a) and 3(c) depict the normalized atomic population as a function of distance from the solid/liquid interface, accompanied by the corresponding top views of atom positions shown in Figs. 3(b) and 3(d). In Figs. 3(a) and 3(c), it can be observed that the peak concentration of Cu/Zr decreases, approaching that of the supercooled liquid over approximately five atomic layers. This behavior allows us to extract a correlation length of density peak for Cu/Zr density distribution. The introduction of Al into the system does not result in significant variations in the correlation length of Cu/Zr density distribution.

Our attention now turns to the structure of local atomic packing. Figure 4(a) presents the distributions of normalized density ρ as a function of distance from the crystal layers in the $(ZrCu)_{100-x}Al_x$ alloys ($x = 0$ and 8), revealing nearly identical curves. These density distributions were obtained using the iso-configurational averaging method. The introduction of trace elements has no discernable impact on the macroscopic order. The presence of an icosahedral structure, characterized by five-fold symmetry, creates frustration and competition with crystallization. To quantify the local atomic symmetry, we employed the parameter f_5 defined as $f_5 = n_5/\sum_{i=3}^{6} n_i$, where n_i represents the number of i-edged faces of the Voronoi polyhedron. Figure 4(b) illustrates the normalized sum-f_5 values for each layer as well as the sum atomic f_5 values. Significantly, the normalized sum-f_5 value of $(ZrCu)_{92}Al_8$ increases rapidly in the three closest interface layers, particularly in the third layer. This indicates a larger number of icosahedron-like structures within the interface layers. As the distance from the solid–liquid interface increases (beyond the 3rd layer), the probability of five-fold symmetry clusters gradually approaches the liquid level of $Zr_{50}Cu_{50}$. The addition of a small amount of Al rapidly enhances the presence of five-fold symmetry clusters at the solid–liquid interface, a phenomenon that diminishes with increasing distance from the interface. In Figs. 4(c)–4(f), it can be observed that the addition of Al leads to larger f_5 values for Al and its neighboring atoms. Overall, the minor addition of Al does not alter the density order, but it

does influence the local packing order.

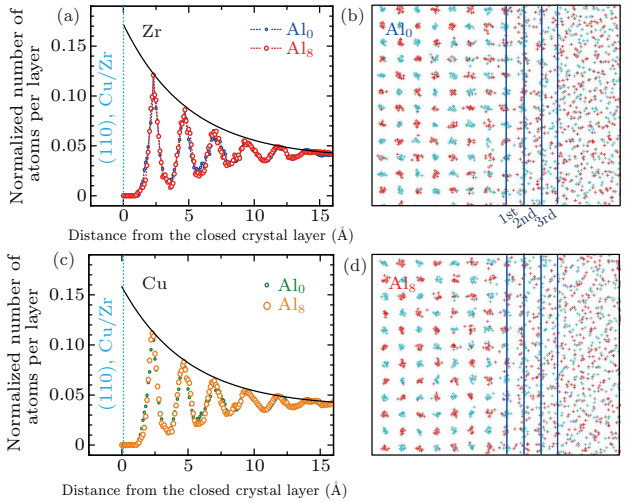


Fig. 3. (a) and (c) The normalized distribution of atoms in the liquid layers near the frozen crystal layers was investigated for two samples of $(ZrCu)_{100-x}Al_x$, with $x = 0$ at a temperature of 1190 K and $x = 8$ at a temperature of 1125 K. (b) and (d) Atomic position map, solid lines are guides for the eye of the layers. The closest three layers from the crystal layer are the 1st, 2nd, and 3rd.

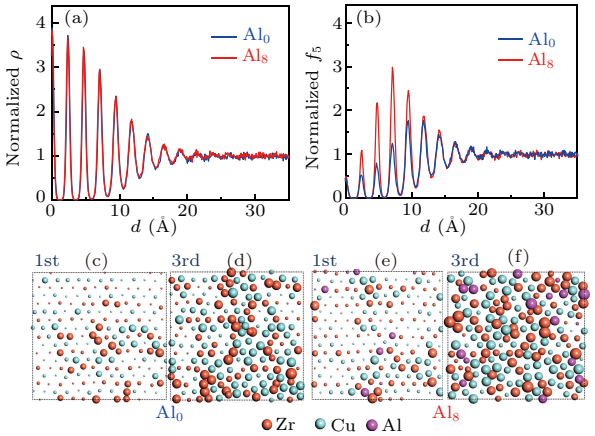


Fig. 4. (a) The normalized density ρ and (b) the normalized five-fold symmetry sum-f_5 as a function of the distance from the crystal layers in $(ZrCu)_{100-x}Al_x$ ($x = 0$ and 8). (c)–(f) Snapshots of the 1st and 3rd layer's atomic f_5 in the $(ZrCu)_{100-x}Al_x$ ($x = 0$, and 8). The atomic radius is proportional to the value of f_5. The orange, lake blue, and purple represent Zr, Cu, and Al, respectively.

3.3. Interface structure with five-fold symmetry formed a network

To analyze the microstructure details of the solid–liquid surface, we employed bond-orientational order (BOO) parameters (q_{lm})[39] to measure the local orientational order between a particle and its neighboring atoms, which can be expressed as

$$q_{lm}(i) = \frac{1}{N_b(i)} \sum_{j=1}^{N_b(i)} Y_{lm}(\theta(r_{ij}), \phi(r_{ij})), \tag{3}$$

where r_{ij} represents the bond between particles i and j, $Y_{lm}(\theta(r_{ij}), \phi(r_{ij}))$ denotes the spherical harmonics of bond r_{ij} with l degree and m order, and $N_b(i)$ represents the number of the first nearest neighbor of particle i.

$$q_l(i) = \sqrt{\frac{4\pi}{2l+1} \sum_{m=-l}^{l} |q_{lm}(i)|^2}, \tag{4}$$

$$Q_{lm}(i) = \frac{1}{1+N_b(i)} \left[q_{lm}(i) + \sum_{j=1}^{N_b(i)} q_{lm}(j) \right]. \tag{5}$$

It is common to utilize multiple BOO to characterize a particle's local environment. The coarse-grained $Q_{lm}(i)$ is used to differentiate between different ordered environments and reduce the overlap between two different BOO parameter maps.[40] The plot of Q_4 against Q_6 is commonly employed to distinguish between disordered (liquid-like) and ordered (crystal-like) environments. Figure 5(a) demonstrates that $Zr_{50}Cu_{50}$ exhibits a connected structure in the interface layers, indicating a cohesive atomic environment surrounding the solid–liquid interface in $Zr_{50}Cu_{50}$. However, in the case of $(ZrCu)_{92}Al_8$, a distinct boundary appears in the same region, as depicted in Fig. 5(b). The addition of Al induces a significant alteration in the atomic packing structure, leading to the emergence of a new structure, as evidenced by an additional boundary line in the Q_4–Q_6 interface plot.

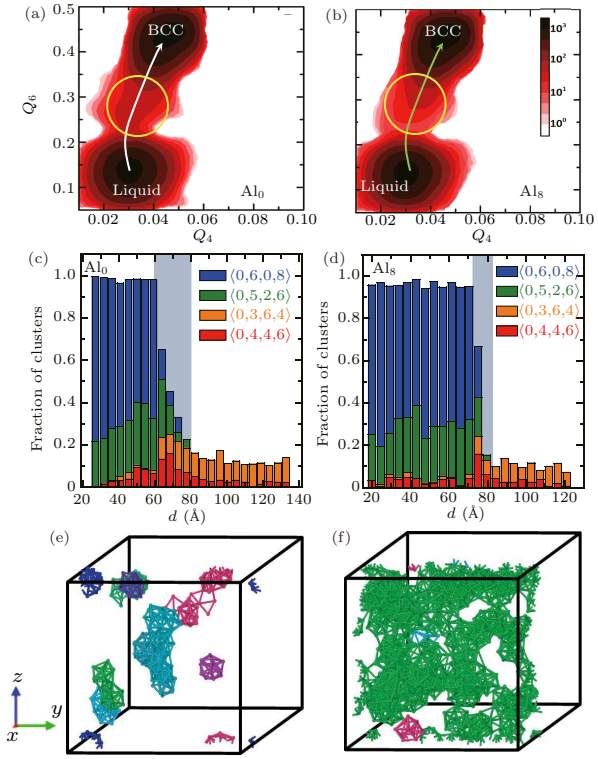


Fig. 5. (a) and (b) The contour plots for Q_4 and Q_6 in $(ZrCu)_{100-x}Al_x$ ($x = 0$ and 8). The yellow circles represent the distinguishing contour plot difference for Q_4 and Q_6 values of the sample with $x = 0$ and $x = 8$. The yellow circles are for eye guidance only. (c) and (d) The fraction of four dominant ordered Voronoi polyhedral types with the distance from the fixed layer in the z-axis of $(ZrCu)_{100-x}Al_x$ ($x = 0$ and 8) at 1050 K. The gray area represents the width of layers where the ordered structure decays. Panels (e) and (f) show the cluster analysis of icosahedrons at the interfaces for $x = 0$ and $x = 8$ at 950 K, respectively.

To further characterize the microstructure, we employed the Voronoi index. Figures 5(c) and 5(d) present the proportions of the four dominant ordering Voronoi polyhedral in $Zr_{50}Cu_{50}$ and $(ZrCu)_{92}Al_8$, respectively, along the crystal growth direction at 1050 K. At the solid–liquid interface, the

crystal order content of $Zr_{50}Cu_{50}$ gradually decreases while maintaining good connectivity in the subsequent layers. In contrast, the crystal order of $(ZrCu)_{92}Al_8$ sharply drops to less than 20% within one interface layer, resulting in a rapid accumulation of B2-unfavorable motifs. In CuZr-based MGs, these two competing structures, crystal order and B2-unfavorable motifs, have been observed to exhibit significantly different temperature response behaviors.[29,31,41] These changes impede further progress in the crystallization process. We performed a cluster-linking analysis on the icosahedral structures at the interface, as illustrated in Figs. 5(e) and 5(f). The results revealed that when $x = 8$, nearly all icosahedra at the interface are interconnected, forming predominantly uniform clusters of the same type. In contrast, when $x = 0$, the density of icosahedra is significantly lower, and they are spatially dispersed. According to Fig. 5(e), when the icosahedral-like network structure at the interface has a lower degree of connectivity, the connectivity between the crystalline surface layer and the liquid phase is not blocked, and the interface region contains a large number of B2-favorable motifs that exhibit characteristics of the liquid-to-crystal phase transition (as shown in the gray area of the 6 nm–8 nm region in Fig. 5(c)), which facilitates continued crystal growth. In contrast, when the network connectivity of the B2-unfavorable motifs, such as icosahedral motif, is higher, the crystalline surface layer is effectively separated from the liquid phase, leading to a significant reduction in B2-favorable motifs with liquid-to-crystal phase transition characteristics (as shown in the gray area of the 7.5 nm–8 nm region in Fig. 5(d)), thus effectively preventing the growth of the crystalline interface.

This behavior is especially prominent at deep supercooled temperatures in $(ZrCu)_{92}Al_8$. Figure 6(a) illustrates the composition of the B2-unfavorable motifs: icosahedron $\langle 0,0,12,0\rangle$, icosahedral precursor $\langle 0,2,8,2\rangle$, and the two B2-favorable motifs: $\langle 0,6,0,8\rangle$, $\langle 0,5,2,6\rangle$ along the z-axis direction of $(ZrCu)_{92}Al_8$ at 950 K. The presence of the icosahedral structure and its precursors, which exhibit a high degree of five-fold symmetry, rapidly increases to 70% in the layer immediately following the solid–liquid interface. These structures can act as network modifiers, introducing structural disorder and promoting glass formation. As a result, the crystallization behavior becomes almost stagnant, leading to a substantial drop in the crystallization rate as depicted in Fig. 1(c) for $(ZrCu)_{92}Al_8$ at supercooled temperatures. In Fig. 6(b), we plotted the distributions of Q_6 and w_6 for the B2-unfavorable motifs and B2-favorable motifs in $(ZrCu)_{92}Al_8$ at 950 K.

$$w_l(i) = \sum_{m_1 m_2 m_3 = 0}^{l} \begin{pmatrix} l & l & l \\ m_1 & m_2 & m_3 \end{pmatrix} \frac{q_{lm1}(i) q_{lm2}(i) q_{lm3}(i)}{|q_l(i)|^3}. \quad (6)$$

The diagonal distributions suggest that the two structures possess entirely different trends in the bond orientation BOO map.

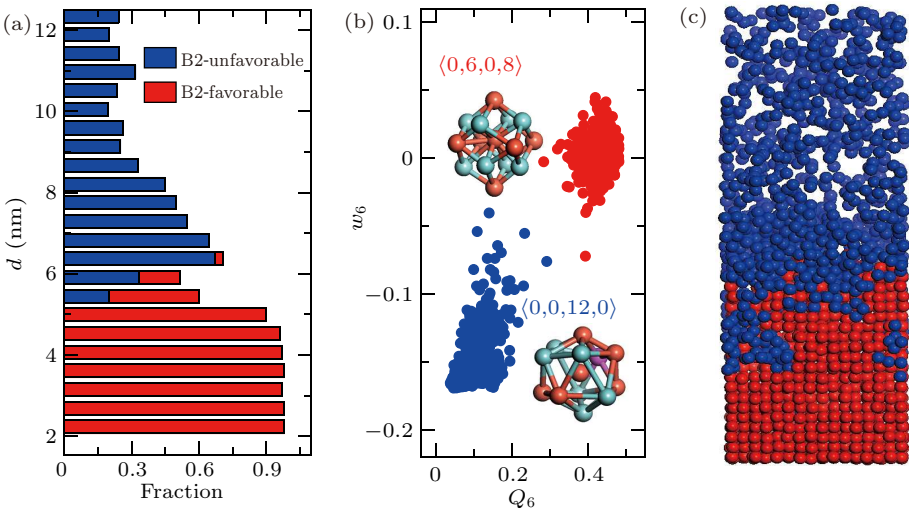


Fig. 6. (a) The fraction of B2-unfavorable motif ($\langle 0,0,12,0\rangle$ and $\langle 0,2,8,2\rangle$) and B2-favorable motif ($\langle 0,6,0,8\rangle$ and $\langle 0,5,2,6\rangle$) Voronoi polyhedral with the distance from the fixed layer in $(ZrCu)_{92}Al_8$ at 950 K. (b) The value of w_6 and Q_6 of the $\langle 0,0,12,0\rangle$ and $\langle 0,6,0,8\rangle$ Voronoi polyhedral. (c) The snapshot of the B2-unfavorable motif and B2-favorable motif of $(ZrCu)_{92}Al_8$ at 950 K.

Figure 6(c) visualizes the spatial distribution of B2-unfavorable motif and B2-favorable motif. At a deep supercooled temperature, the solid–liquid interface of $(ZrCu)_{92}Al_8$ rapidly fills with B2-unfavorable motifs with near-total five-fold symmetry, blocking the continued growth of crystals and enhancing the GFA. The increase in icosahedral order near the interface can be attributed to two main factors: (i) the addition of Al significantly reduces the formation energy of $\langle 0,0,12,0\rangle$-like motif, as previously proposed; (ii) the wall-pinning effect induced by the interface leads to a significant slowdown in dynamics near the interface.[42] This slowdown indicates a lower effective temperature in the interfacial region, which provides more favorable conditions for the formation of icosahedral clusters. Additionally, the aggregation of icosahedral clusters further increases viscosity, promoting the formation of more icosahedral clusters. Ultimately, a dense

network is woven near the interface, preventing the growth of the crystalline phase.

4. Discussion

To achieve a more comprehensive understanding of minor alloying element effect of glass forming ability of metallic melts, we employed the forward flux sampling (FFS)[43,44] technique to study the nucleation processes of two glass-forming liquids with different compositions: $Zr_{50}Cu_{50}$ and $Zr_{46}Cu_{46}Al_8$, in addition to the aforementioned growth processes. The simulated temperature was set at 1050 K, corresponding to the fastest growth rate shown in Fig. 1(b). Based on the bond orientational order (BOO) parameter $S_l(i,j)$,[40,45] we propose using the averaged BOO parameter $\bar{S}_l(i,j)$ to distinguish between solid and liquid:

$$\tilde{Q}_{lm}(i) = \frac{Q_{lm}(i)}{\left(\sum_{m=-l}^{l} |Q_{lm}(i)|^2\right)^{1/2}}, \tag{7}$$

$$\bar{S}_l(i,j) = \sum_{m=-l}^{l} \tilde{Q}_{lm}(i)\,\tilde{Q}^*_{lm}(j), \tag{8}$$

where $Q_{lm}(i)$ is defined by Eq. (5), and we set $l = 6$. Two particles i and j are defined to be connected if $\bar{S}_6(i,j) > 0.89$, and particle i is considered solid-like if its number of connections is greater than or equal to 7. Ultimately, we count the number of atoms in the largest cluster composed of solid-like atoms as the parameter λ. To study the rate k_{AB} of the system's evolution from λ_A to λ_B ($\lambda_A < \lambda_B$), FFS inserts additional interfaces $\lambda_A \le \lambda_0 < \lambda_1 < \cdots < \lambda_n = \lambda_B$ between λ_A and λ_B. Consequently, the rate k_{AB} can be expressed as[43]

$$k_{AB} = \frac{\bar{\Phi}_{A,0}}{\bar{h}_{\mathcal{A}}} \prod_{i=0}^{n-1} P(\lambda_{i+1}\,|\,\lambda_i), \tag{9}$$

where $\bar{\Phi}_{A,0}$ represents the average flux from λ_A to λ_0, the factor $\bar{h}_{\mathcal{A}}$ represents the average time the system spends in the "attractive basin" A, and $P(\lambda_{i+1}|\lambda_i)$ represents the probability of proceeding to λ_{i+1} after reaching λ_i rather than returning to λ_A. Furthermore, we utilize the temporally coarse-grained FFS[44] and increase the sampling time to 1 ps to filter out undesirable high-frequency fluctuations.

Figure 7 illustrates the simulated crystal nucleus growth probability for investigated compositions. Contrary to the growth process discussed earlier, $Zr_{46}Cu_{46}Al_8$ exhibits a significantly higher nucleation rate compared to $Zr_{50}Cu_{50}$. Upon examining the specific morphology of the nuclei, it was found that both alloys formed the Laves phase rather than the B2 phase. This finding agrees with a previous study that reported the formation of the Laves phase in $Zr_{46}Cu_{46}Al_8$ through extensive MD simulations[46] based on the same EAM potential.[33] This indicates that the addition of Al enhances local five-fold symmetry in the ZrCu melt, facilitating the formation of the Laves phase, which incorporates Cu-centered icosahedral motifs. The inhibition of B2 crystalline phase growth observed in interface growth simulations, attributed to the enhanced icosahedral network at the interface, may stem from the competition between the matrix B2 phase and the Laves phase, which tends to nucleate in the supercooled liquid. Regardless of the specific mechanism driving the increase in B2-unfavorable motifs at the interface, this phenomenon ultimately alters the structural evolution pathway and elevates the activation energy barrier,[47,48] thereby complicating the crystalline growth process. Consequently, regulating the topological stacking at the crystal–liquid interface through trace element addition emerges as an effective strategy for optimizing glass-forming ability. Achieving accurate representation of trace element effects in simulations, however, necessitates the use of high-precision interatomic potentials, such as machine-learning-based potentials.[49,50]

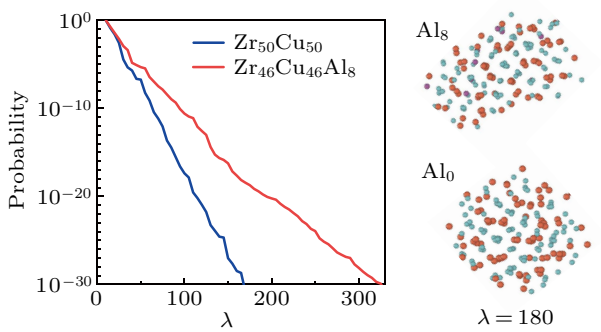


Fig. 7. Crystal nucleus growth probability at 1050 K for glass-forming liquids $Zr_{50}Cu_{50}$ and $Zr_{46}Cu_{46}Al_8$. The snapshots at nuclear size $\lambda = 180$ are shown on the right.

In this study, we utilize the ZrCuAl system as a model to investigate how trace additions of Al influence the crystallization rate by modulating the properties of the crystal–liquid interface, thereby impacting the glass-forming ability (GFA). Unlike previous findings in various alloy systems, where differences in crystallization ability could be inferred from the decay of atomic density fluctuations, the addition of trace amounts of Al does not alter the density fluctuation decay in the interfacial region. Nevertheless, it leads to a substantial reduction in the crystallization rate, by several orders of magnitude compared to the ZrCu alloy system. Detailed analysis of the local structure reveals that even a small amount of Al modifies the motifs in the interfacial region. These motifs transition from crystal-phase-favorable motifs, which typically form under the influence of the crystalline field, to $\langle 0,0,12,0\rangle$ motifs, which are unfavorable for crystal growth. This shift increases the energy barrier for crystal growth, thereby reducing the growth rate. The underlying mechanism is that Al addition significantly lowers the formation energy of $\langle 0,0,12,0\rangle$ motifs. The formation role of motifs is governed by the cooperative interactions among elements. It underscores the inherent challenges and complexities of composition-dependent

GFA in alloys, warranting systematic investigation using AI-associated large-scale atomic models in future studies.

In summary, the introduction of minor elements led to a filling of the solid–liquid interface with crystal-unfavorable motifs, which is significantly higher than that in the bulk liquid under the same bath temperature, impeding the formation pathway of crystalline-like order. These structures with five-fold symmetry formed a network, hindering the formation and growth of crystalline order. This effect was particularly pronounced at deep supercooled temperatures, reminiscent of a pinning effect[51] that reduced structural rearrangement, increased the content of icosahedra, and ultimately improved the system's GFA. Therefore, the effect of trace element addition is not limited to a modest increase in crystal-unfavorable motifs within the bulk supercooled liquid. More importantly, it leads to a significant enhancement of such motifs at the crystal–supercooled liquid interface, which provides critical insights that cannot be obtained solely from studies of bulk supercooled liquids. This finding offers a potential approach for the preliminary assessment of glass-forming ability (GFA) in simulations. By comparing the differences in motifs between the interfacial region and the crystal phase, a qualitative evaluation of GFA may be achievable.

Acknowledgements

Project supported by the National Natural Science Foundation of China (Grant Nos. T2325004 and 52161160330). Shan Zhang and Pengfei Guan acknowledge the computational support from the Beijing Computational Science Research Center (CSRC). Yong Yang acknowledges the support from the Hong Kong Institute of Advanced Studies through the materials cluster project.

References

[1] Schroers J 2013 *Phys. Today* **66** 32
[2] Trexler M M and Thadhani N N 2010 *Prog. Mater. Sci.* **55** 759
[3] Huo J, Li K, Zang B, Gao M, Wang L M, Sun B, Li M, Song L, Wang J Q and Wang W H 2022 *Chin. Phys. Lett.* **39** 046401
[4] Lu T, Liu S L, Sun Y H, Wang W H and Pan M X 2022 *Chin. Phys. Lett.* **39** 036401
[5] Gao M H, Lu W Y, Yang B J, Zhang S D and Wang J Q 2018 *J. Alloys Compd.* **735** 1363
[6] Li F C, Liu T, Zhang J Y, Shuang S, Wang Q, Wang A D, Wang J G and Yang Y 2019 *Mater. Today Adv.* **4** 100027
[7] Zhang H R, Mei X X, Zhang X N, Li X N, Wang Y M, Sun J R and Wang Y N 2016 *Nucl. Instrum. Methods Phys. Res., Sect. B* **375** 79
[8] Li H X, Lu Z C, Wang S L, Wu Y and Lu Z P 2019 *Prog. Mater. Sci.* **103** 235
[9] Mukherjee S, Carmo M, Kumar G, Sekol R C, Taylor A D and Schroers J 2012 *Electrochim. Acta* **74** 145
[10] Jia Z, Duan X G, Qin P, Zhang W C, Wang W M, Yang C, Sun H Q, Wang S B and Zhang L C 2017 *Adv. Funct. Mater.* **27** 1702258
[11] Greer A L 2015 *Nat. Mater.* **14** 542
[12] Inoue A 2000 *Acta Mater.* **48** 279
[13] Nie Y, Liu J, Guo J and Xu N 2020 *Nat. Commun.* **11** 3198
[14] Lu Z P and Liu C T 2003 *Phys. Rev. Lett.* **91** 115505
[15] Ma L, Yang X D, Yang F, Zhou X J and Wu Z W 2024 *Chin. Phys. B* **33** 036402
[16] Lu Z P and Liu C T 2002 *Acta Mater.* **50** 3501
[17] Wang W H, Bian Z, Wen P, Zhang Y, Pan M X and Zhao D Q 2002 *Intermetallics.* **10** 1249
[18] Yang L, Guo G Q, Chen L Y, Huang C L, Ge T, Chen D, Liaw P K, Saksl K, Ren Y, Zeng Q S, Laqua B, Chen F G and Jiang J Z 2012 *Phys. Rev. Lett.* **109** 105502
[19] Wang J, Liu X, Wu Y, Wang H, Ma D and Lu Z 2023 *Acta Mater.* **261** 119386
[20] Wang J Q, Liu Y H, Imhoff S, Chen N, Louzguine-Luzgin D V, Takeuchi A, Chen M W, Kato H, Perepezko J H and Inoue A 2012 *Intermetallics.* **29** 35
[21] Wu N C, Zuo L, Wang J Q and Ma E 2016 *Acta Mater.* **108** 143
[22] Zai W, Man H C, Su Y C, Li G Y and Lian J S 2020 *Mater. Chem. Phys.* **255** 123555
[23] Zhang Q, Zhang W and Inoue A 2006 *Scripta Mater.* **55** 711
[24] Yu P, Bai H Y and Wang W H 2006 *J. Mater. Res.* **21** 1674
[25] Zhang B, Zhao D Q, Pan M, Wang R J and Wang W H 2006 *Acta Mater.* **54** 3025
[26] Xue L, Shao L L, Luo Q, Hu L N, Zhao Y B, Yin K B, Zhu M Y, Sun L T, Shen B L and Bian X F 2021 *J. Mater. Sci. Technol.* **77** 28
[27] Kim H K, Ahn J P, Lee B J, Park K W and Lee J C 2018 *Acta Mater.* **157** 209
[28] Liu Q L, Mo J Y, Liu H S, Xue L, Hou L, Yang W M, Dou L T, Shen B L and Dou L M 2016 *J. Non-Cryst. Solids* **443** 108
[29] Kim H K, Lee M, Lee K R and Lee J C 2013 *Acta Mater.* **61** 6597
[30] Shao L L, Wang Q Q, Xue L, Zhu M Y, Wang A D, Luan J H, Yin K B, Luo Q, Zeng Q S, Sun L T and Shen B L 2021 *J. Mater. Res. Technol.* **11** 378
[31] Hu Y C and Tanaka H 2020 *Sci. Adv.* **6** eabd2928
[32] Thompson A P, Aktulga H M, Berger R, Bolintineanu D S, Brown W M, Crozier P S, In'T Veld P J, Kohlmeyer A, Moore S G, Nguyen T D, Shan R, Stevens M J, Tranchida J, Trott C and Plimpton S J 2022 *Comput. Phys. Commun.* **271** 108171
[33] Cheng Y Q, Ma E and Sheng H W 2009 *Phys. Rev. Lett.* **102** 245501
[34] Tang C and Harrowell P 2013 *Nat. Mater.* **12** 507
[35] Wilson H W 1900 *London, Edinburgh Dublin Philos. Mag. J. Sci.* **50** 238
[36] Frenkel J 1946 *Kinetic theory of liquids* (Oxford University Press)
[37] Hao S G, Wang C Z, Kramer M J and Ho K M 2010 *J. Appl. Phys.* **107** 053511
[38] Yang Y, Humadi H, Buta D, Laird B B, Sun D, Hoyt J J and Asta M 2011 *Phys. Rev. Lett.* **107** 025505
[39] Tanaka H, Tong H, Shi R and Russo J 2019 *Nat. Rev. Phys.* **1** 333
[40] Lechner W and Dellago C 2008 *J. Chem. Phys.* **129** 114707
[41] Tanaka H 2003 *J. Phys.: Condens. Matter.* **15** L491
[42] Hu Y C, Li Y W, Yang Y, Guan P F, Bai H Y and Wang W H 2018 *Proc. Natl. Acad. Sci. USA* **115** 6375
[43] Allen R J, Frenkel D and Ten Wolde P R 2006 *J. Chem. Phys.* **124** 024102
[44] Hussain S and Haji-Akbari A 2020 *J. Chem. Phys.* **152** 060901
[45] Ten Wolde P R, Ruiz-Montero M J and Frenkel D 1996 *Faraday Discuss.* **104** 93
[46] Ryltsev R E, Klumov B A, Chtchelkatchev N M and Shunyaev K Y 2018 *J. Chem. Phys.* **149** 164502
[47] Yan Z, Sheng H, Ma E, Xu B, Li J and Kong L 2021 *Acta Mater.* **202** 387
[48] Mao Y, Li J, Lo Y C, Qian X and Ma E 2015 *Phys. Rev. B* **91** 214103
[49] Li F, Zhang Z, Liu H, Zhu W, Wang T, Park M, Zhang J, Bönninghoff N, Feng X, Zhang H, Luan J, Wang J, Liu X, Chang T, Chu J P, Lu Y, Liu Y, Guan P and Yang Y 2024 *Nat. Mater.* **23** 52
[50] Su R, Yu J, Guan P F and Wang W H 2024 *Sci. China-Mater.* **67** 3298
[51] Wang Q, Liu C T, Yang Y, Dong Y D and Lu J 2011 *Phys. Rev. Lett.* **106** 215505